Acceleration and deceleration of coronal mass ejections during propagation and interaction

Fang Shen,[1,2] S. T. Wu,[2] Xueshang Feng,[1] and Chin-Chun Wu[3]

Received 28 March 2012; revised 9 September 2012; accepted 21 September 2012; published 2 November 2012.

[1] A major challenge to the space weather forecasting community is accurate prediction of Coronal Mass Ejections (CMEs) induced Shock Arrival Time (SAT) at Earth's environment. In order to improve the current accuracy, one of the steps is to understand the physical processes of the acceleration and deceleration of a CME's propagation in the heliosphere. We employ our previous study of a three-dimensional (3D) magnetohydrodynamic (MHD) simulation for the evolution of two interacting CMEs in a realistic ambient solar wind during the period 28–31 March 2001 event to illustrate these acceleration and deceleration processes. The forces which caused the acceleration and deceleration are analyzed in detail. The forces which caused the acceleration are the magnetic pressure term of Lorentz force and pressure gradient. On the other hand, the forces which caused the deceleration are aerodynamic drag, the Sun's gravity and the tension of magnetic field. In addition the momentum exchange between the solar wind and the moving CMEs can cause acceleration and deceleration of the CME which are now analyzed. In this specific CME event 28–31 March 2001 we have analyzed those forces which cause acceleration and deceleration of CME with and without interaction with another CME. It shows that there are significant momentum changes between these two interacting CMEs to cause the acceleration and deceleration.

Citation: Shen, F., S. T. Wu, X. Feng, and C.-C. Wu (2012), Acceleration and deceleration of coronal mass ejections during propagation and interaction, *J. Geophys. Res.*, *117*, A11101, doi:10.1029/2012JA017776.

1. Introduction

[2] With the improvement of coronagraphic observations and the presence of the solar wind measurement in the outer heliosphere (Voyager, Ulysses), it is believed that successive ICMEs can merge with each other and form a compound structure, as mentioned formerly [e.g., *Burlaga et al.*, 2002; *Lugaz and Roussev*, 2011]. The same phenomenon also happens in the inner heliosphere, before CMEs reach Earth. When two or more ejections interact, they can form the well-known multiple ICME or magnetic cloud structure [*Wang et al.*, 2002, 2003]. These CMEs interactions result in different solar wind signatures as well as different geoeffectiveness as compared to isolated CME events. Numerical simulations, which yield the observed complexity, are useful to understand and determine the dynamical evolutionary processes of the CMEs interactions. Recently, *Shen et al.* [2011b] have investigated the characteristics of two CMEs from 28 March 2001 event during their propagation and interaction, but they have not analyzed the detailed forces to cause the acceleration and deceleration of the interacting CMEs.

[3] It has been known observationally that CMEs show two distinct speed-height profiles according to many investigators [*MacQueen and Fisher*, 1983; *Sheeley et al.*, 1999; *St. Cyr et al.*, 1999; *Andrews and Howard*, 2001]. CMEs that originate from an active region accompanied by a flare usually have an initial speed well above the CME medium speed of 400 km s^{-1} and are referred to as fast CMEs or constant speed CMEs [*MacQueen and Fisher*, 1983]. These CMEs show no significant acceleration, but may show some deceleration [*St. Cyr et al.*, 2000]. There are other kinds of CMEs that originate above a quiescent prominence, away from active regions which have an initial speed much less than the medium speed and are referred to as slow CMEs. These CMEs show a gradual acceleration which may attain higher speeds and are called accelerated CMEs. *Low and Zhang* [2002] suggested that these two classes of CMEs could be a result of a difference in the initial topology of the magnetic fields associated with the underlying quiescent prominences, viz, the normal and inverse magnetic configuration [*Tandberg-Hanssen*, 1995]. These two types of CMEs were simulated by *Wu et al.* [2004, 2005] using their 2.5D, time-dependent streamer and flux-rope MHD model [*Wu and Guo*, 1997] based on both inverse and normal

[1]SIGMA Weather Group, State Key Laboratory of Space Weather, Center for Space Science and Applied Research, Chinese Academy of Sciences, Beijing, China.
[2]CSPAR and Department of Mechanical and Aerospace Engineering, University of Alabama, Huntsville, Alabama, USA.
[3]Naval Research Laboratory, Washington, D. C., USA.

Corresponding author: F. Shen, SIGMA Weather Group, State Key Laboratory of Space Weather, Center for Space Science and Applied Research, Chinese Academy of Sciences, Beijing 100190, China. (fshen@spaceweather.ac.cn)

0148-0227/12/2012JA017776

quiescent prominence topology to analyze the forces acting on a single CME, respectively. They showed that the inverse magnetic topology could also produce a fast CME with a specific initial process. *Wang et al.* [2005] have investigated the CME-CME interaction according to the observed 20 January 2001 CME-CME interaction event, they found that CME cannibalism is caused by the magnetic reconnection. *Chen and Krall* [2003] analyzed the CME acceleration processes using a theoretical model of CMEs based on a 3D magnetic flux rope to find that the CMEs acceleration has a universal scaling law which is related to a critical height that the maximum acceleration is attained.

[4] It is well known that the major force that propels CMEs into the solar wind is the Lorentz force [*Chen*, 1989, 1996; *Vršnak*, 2006] and the restraining force is mainly the aerodynamic drag [*Vršnak and Glpalswamy*, 2002; *Cargill*, 2004]. *Cargill et al.* [1996] investigated the aerodynamic effects coupling with background solar wind to analyze the CME acceleration and deceleration using a flux-rope driven through the magnetized plasma. The numerical simulation of the transport of ICMEs has been investigated extensively [e.g., *Cargill et al.*, 1996; *Cargill*, 2004; *González-Esparza et al.*, 2003; *Chen*, 1996; *Borgazzi et al.*, 2009]. They generally study the propagation, through the interplanetary space, of some properties (temperature, density and speed) of the ICMEs. *Manchester et al.* [2004] have studied numerically the kinematics and forces acting on a simulated CME. Most recently, *Joshi and Srivastava* [2011] studied the acceleration of CMEs using 3D reconstruction of CMEs observed by STEREO, they found that the CME leading edge undergoes maximum acceleration typically below 2 R_s, but the associated prominence CMEs show acceleration up to a height of $\sim$4 R_s. After collision of two interplanetary features, it is normal that the faster one is decelerated but the slower one is accelerated. Recently, *Temmer et al.* [2012] have investigated the deceleration of two CMEs interaction using a drag-based model [*Vršnak et al.*, 2012], based on 1 August 2010 events observed by STEREO SECCHI. They have found that the magnetic forces may contribute to the enhanced deceleration of CME2; and the increase in magnetic tension and pressure, when CME2 bends and compresses the magnetic field lines of CME1, increases the efficiency of drag.

[5] In this study, we will present a force analysis based on our recently published results [*Shen et al.*, 2011b] for two CMEs interaction for 28–31 March 2001 event to examine the acceleration and deceleration of a single CME and the interaction of two CMEs with inverse type magnetic field topology, respectively, using a 3D MHD simulation. These two CMEs are mimicked by two opposite polarity plasma blobs, which is identical to our previous study [*Shen et al.*, 2011b]. In this type magnetic topology, the reconnection will not appear.

[6] The paper is organized as follows: the simulation model is described in section 2 and the numerical results are given in section 3. The summary and discussion are included in section 4.

2. Description of the Simulation Model

[7] In our previous study, we have constructed a 3D time-dependent, numerical MHD model (COIN-TVD MHD model) to investigate the evolution and interaction of two CMEs in the nonhomogeneous ambient solar wind. The background solar wind is constructed based on the self-consistent source surface [*Wei et al.*, 2003; *Shen et al.*, 2010, 2012] with observed line-of-sight of magnetic field and density from the source surface of 2.5 R_s to the Earth's orbit (215 R_s) and beyond. The detailed description about the computational domain, the grid mesh, the asynchronous and parallel time-marching method, and the self-consistent initial boundary conditions for this 3D MHD simulation are given in *Shen et al.* [2007, 2009, 2011a, 2011b] which will not be repeated here.

[8] In our COIN-TVD MHD model, a modified Total Variation Diminishing/Lax-Friedrichs (TVD/LF) type scheme [*Feng et al.*, 2003, 2005; *Shen et al.*, 2007, 2009, 2011a, 2011b] is applied as the numerical 3D MHD scheme with electric field modification method [*Tóth*, 2000] to assure $\nabla \cdot \vec{B} = 0$. The MHD equations can be written in a spherical-component form at the inertial (nonrotating) reference frame, which was described in detail in our pervious papers [*Shen et al.*, 2007, 2011a, 2011b], and will not be repeated here. The calculated steady state 3D magnetic field topology and radial velocity distribution based on the inputs of measured line-of-sight magnetic field on the source surface are shown in Figure 1 of *Shen et al.* [2011b].

[9] The two successive CMEs occurring on 28 March 2001 and forming a multiple magnetic cloud (multiMC) in interplanetary space were chosen as a test case [*Shen et al.*, 2011b]. Descriptions of this 28 March 2001 event have been reported in our previous paper [*Shen et al.*, 2011b]. Here we'll summarize some of the highlights for this event for completeness. The first halo CME was observed by LASCO/C2 at 01:27 UT on 28 March 2001, located at N20E22. The second halo CME was visible by C2 at 12:50 UT on the same day, located at N18E02. The projected speed of the first CME and the second CME were 427 km/s and 519 km/s, respectively, according to the LASCO CME catalog. Based on the ACE spacecraft observation, a very intense forward shock arrived at the L1 point (1.5×10^9 m from the Earth to sunward) at 00:20 UT on 31 March 2001. Then, the first magnetic cloud was observed from 0505 UT to 1015 UT and the second one was observed during 1235–2140 UT. And the very large geomagnetic strom with a Dst value of -387 nT was caused by this MultiMC event during the 23rd solar maximum (2000–2001) [*Wang et al.*, 2003].

[10] Here, these two successive CMEs are simulated by means of two high-density, high-velocity and high-temperature magnetized plasma blobs model, as first suggested by *Chané et al.* [2005, 2006, 2008], and successively ejected into the nonhomogeneous background solar wind medium along different initial launch directions, respectively [*Shen et al.*, 2011b].

[11] The density, radial velocity and temperature profiles of the initial perturbation are defined as follows:

$$\begin{cases} \rho_{CME}(r,\theta,\phi) = \dfrac{\rho_{\max}}{2}\left(1 - \cos\left(\pi\dfrac{a_{cme} - a(r,\theta,\phi)}{a_{cme}}\right)\right) \\ V_{CME}(r,\theta,\phi) = \dfrac{v_{\max}}{2}\left(1 - \cos\left(\pi\dfrac{a_{cme} - a(r,\theta,\phi)}{a_{cme}}\right)\right) \\ T_{CME}(r,\theta,\phi) = \dfrac{T_{\max}}{2}\left(1 - \cos\left(\pi\dfrac{a_{cme} - a(r,\theta,\phi)}{a_{cme}}\right)\right) \end{cases} \quad (1)$$

Table 1. The Initial Parameters of CME 1 and CME 2

	CME1	CME2
θcme	20°	18°
ϕcme	158°	178°
ρ_{max} (cm^{-3})	1.2×10^9	1.5×10^9
v_{max} (km/s)	1350	1600
T_{max} (K)	4×10^6	5×10^6
ψ_0	2.0	−2.4

where, a_{cme} is the radius of the initial plasma blob, $a(r, \theta, \phi)$ denotes the distance from the center of the initial plasma blob, and (r_{cme}, θ_{cme}, ϕ_{cme}) is the position of the initial blob center. ρ_{max}, v_{max} and T_{max} are the maximum density, radial velocity and temperature in the plasma bubble added on top of the background solar wind, respectively.

[12] The initial magnetic field of the perturbation in r and θ direction can be defined as [*Shen et al.*, 2011a, 2011b]:

$$\begin{cases} B_{r_{CME}}(r,\theta,\phi) = -\dfrac{1}{r^2\sin\theta}\dfrac{\partial\psi(r,\theta,\phi)}{\partial\theta} \\ B_{\theta_{CME}}(r,\theta,\phi) = -\dfrac{1}{r\sin\theta}\dfrac{\partial\psi(r,\theta,\phi)}{\partial r} \end{cases} \quad (2)$$

where

$$\psi(r,\theta,\phi) = \psi_0\left[a(r,\theta,\phi) - a\frac{a_{CME}}{2\pi}\sin\left(\frac{2\pi a(r,\theta,\phi)}{a_{CME}}\right)\right] \quad (3)$$

is the magnetic flux function.

[13] This initial perturbation is given by the following relation:

$$\begin{cases} \rho = \rho_0 + \rho_{CME}(r,\theta,\phi) \\ v_r = v_{r0} + V_{CME}(r,\theta,\phi) \\ T = T_0 + T_{CME}(r,\theta,\phi) \\ B_r = B_{r0} + B_{rCME}(r,\theta,\phi) \\ B_\theta = B_{\theta0} + B_{\theta CME}(r,\theta,\phi) \end{cases} \quad (4)$$

where ρ_0, v_{r0}, T_0, B_{r0} and $B_{\theta0}$ are the background values of the density, radial velocity, temperature, magnetic field in radial direction and in meridional direction.

[14] In our simulation, the radius of the two plasma blobs is chosen to be 0.5 R_s and the center of the initial plasma blobs is situated at 3.5 R_s. The second plasma blob is initiated 10 h after the launch of the first one. The other parameters are given in Table 1.

[15] The corresponding energy inputs of two simulated CMEs are given in Table 2. The second CME is initiated 10 h after the launch of the first one.

3. Numerical Results

[16] In this section, the simulation results are presented. The simulated CME is defined as a region where the relative density $\left(\frac{\rho-\rho_o}{\rho_o}\right)$ is not less than 0.5, in which ρ and ρ_0 denote the CME density and the background solar wind density, respectively. And we also identify the CME front by choosing the location having maximum velocity in front of the flux-rope. Figure 1 show the 2D relative density $\left(\frac{\rho-\rho_o}{\rho_o}\right)$ (a) and radial velocity (b) contours of the constant latitude angle of $\theta = 18°$ at 20 h. From Figure 1, it could be clearly found that most of the high-speed region (which is the low density magnetic ejecta) is not part of the CME as defined by us. What is tracked is the sheath of the CME, not the CME itself. But the CME front which was identified by choosing the location having maximum velocity in front of the flux-rope is absolutely located inside the CME region we defined.

[17] The forces acting on a unit volume with density ρ can be written in detail as below [*Cargill*, 2004; *Chen and Krall*, 2003; *Wu et al.*, 2004]: (1) The Lorentz force, $F_L = \frac{1}{4\pi}\left(\nabla\times\vec{B}\right)\times\vec{B} = -\nabla\left(\frac{|B|^2}{8\pi}\right) + \frac{1}{4\pi}\left(\vec{B}\cdot\nabla\right)\vec{B}$; the first, $-\nabla\left(\frac{|B|^2}{8\pi}\right)$, can be thought of as due to a gradient of magnetic pressure $\frac{|B|^2}{8\pi}$; and the second part, $\frac{1}{4\pi}\left(\vec{B}\cdot\nabla\right)\vec{B}$, is magnetic tension; (2) The pressure gradient, $F_p = -\nabla p$; (3) the aerodynamic drag force, $F_D = -\rho_e A C_D(V_i - V_e)|V_i - V_e|/\tau$; (4) the gravitational force, $F_g = -\nabla\phi$, where τ and A are the volume and the cross-sectional area of the CME, C_D is the drag coefficient and subscript i, e refers to quantities inside and external, to the CME, respectively. In our simulation, C_D is set as 1.0 [*Cargill*, 2004; *Cargill et al.*, 1994; *Schmidt and Cargill*, 2000; *Temmer et al.*, 2012]. τ is the volume which is defined as being a region where the relative density is not less than 0.5. ϕ is the gravitational potential. Here, we only studied the forces on radial direction attribution to the acceleration and deceleration of the CMEs on radial direction. And the r-component of the pressure gradient at point (i, j, k) is determined by: $(\nabla p)_r = \frac{p(i,j,k)-p(i-1,j,k)}{r(i)-r(i-1)}$. The total force f acting on a unit volume is given as: $f = F_L + Fp + F_D + F_g$. The forces are calculated at every 45 min.

[18] Based on the paper by *Vourlidas et al.* [2010], the total mass of a CME usually reaches a constant at a height about 10 Rs. The mass will not change after a certain height, meaning the conservation of mass. But, the density of CME is varied with time. Thus, we estimate these forces using the CME density similar to the volume-force mentioned by *Vršnak* [2006].

3.1. Case 1: A Single CME

[19] In the first part of this section, we present the simulated results for the single CME case (i.e., only CME1). The initial parameters can be found in Table 1, and the energy input is shown in Table 2. It should be pointed out that the value of the initial magnetic energy is only 4% of the total energy input, which is much smaller than the typical (observed) CMEs.

[20] Figure 2 shows the curves that portray (a) distance-time profiles (b) the radial speed-time profile and (c) the

Table 2. The Corresponding Energy Inputs of CME 1 and CME 2

	CME1	CME2
Magnetic Energy (erg)	3.89×10^{29}	6.60×10^{29}
Gravitational Energy (erg)	8.07×10^{29}	1.41×10^{30}
Thermal Energy (erg)	2.34×10^{30}	4.22×10^{30}
Kinetic Energy (erg)	5.47×10^{30}	1.11×10^{31}
Total Energy (erg)	9.01×10^{30}	1.74×10^{31}

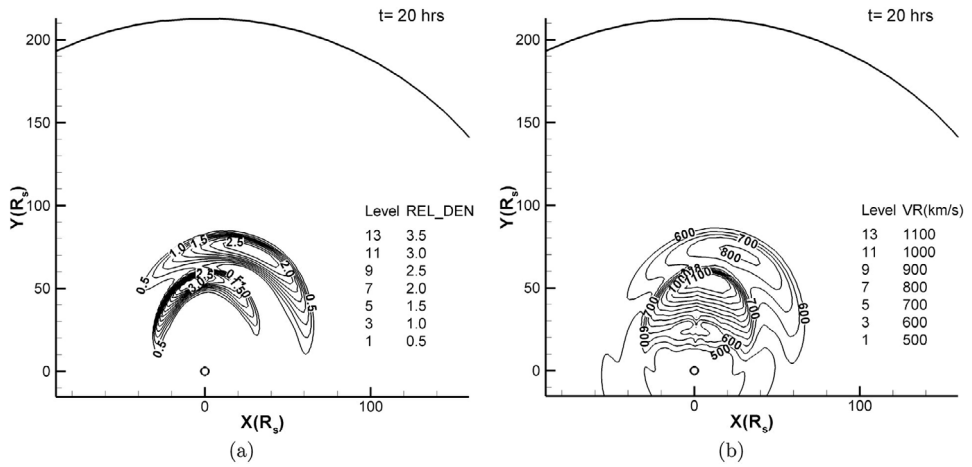

Figure 1. The two-dimensional relative density $((\rho - \rho_0)/\rho_0)$ (a) and radial velocity (b) contours of the constant latitude angle of $\theta = 18^\circ$ at $t = 20$ h (Unit of the axis: R_s).

speed-distance profile of the CME. The radial speed of the CME declines from its birth to near 1 AU.

[21] Figure 3 shows a detailed breakdown of the radial forces attributing to the acceleration and deceleration of the single CME, among which the Lorentz force is split up into the magnetic pressure and the magnetic tension. The black curve is the total force of the pressure, Lorentz force, drag force and gravitational force acting on the CME. In the earlier time (<1 h), the total force is negative. As the CME propagates into the heliosphere, all the forces become small. The total force remains negative (Sunward) all the time, which is consistent with the declining speed curve in Figure 3.

3.2. Case 2: Interaction of Two CMEs

[22] In this section, we present simulation results for the interaction of two CMEs.

[23] Figure 4 shows the curves that portray (a) the distance-time profiles (b) the radial speed-time profile and (c) the speed-distance profile of the two CMEs interaction effects from $t = 0$ to 60 h. The second eruption is initiated 10 h after the launch of the first one. The first in contact is ~30 h (see Figure 5e and 6e in *Shen et al.* [2011b]). At ~40 h, CME2 catch up with CME1. Because the CMEs' initial speeds are much higher than the ambient solar wind speed, at the initial time, both of the two CMEs transfer momentum to solar wind, and they begin to decelerate rapidly. At ~37 h, the two CMEs get closer, while the speed of CME1 is less than that of CME2. CME1 gains momentum from CME2, then, CME1 begins to accelerate from 37 h to 45 h and after 45 h, both of them decelerate together. This momentum transfer is same as what happened due to the momentum conservation (snow-plow model) proposed by *Tappin* [2006]. As the faster, denser CME2 propagates near CME1, it slows down due to the interaction with CME1 by the momentum transfer, and then the slower CME1 ahead of it is accelerated.

[24] The solid lines with different colors in Figure 5 and Figure 6 show the detailed breakdown of the six forces in the radial direction which contributes to the acceleration and deceleration of CME1 and CME2, respectively, at different time intervals from the initiation. The black curves in Figure 5 and Figure 6 show the sum of all the forces which represent the total force acting on CME1 and CME2, respectively. In the earlier stage of the evolution, the total force is dominated by the positive pressure gradient and the negative aerodynamic drag force, especially the drag force, because the CME speed is much faster than the solar wind

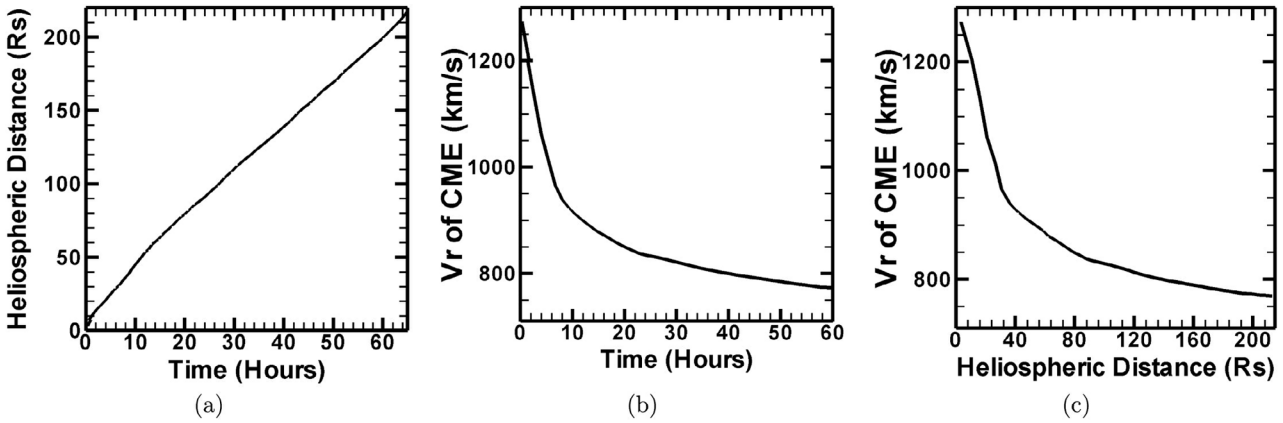

Figure 2. Simulation of (a) CME distance versus time; (b) CME radial speed versus time and (c) CME radial speed versus distance.

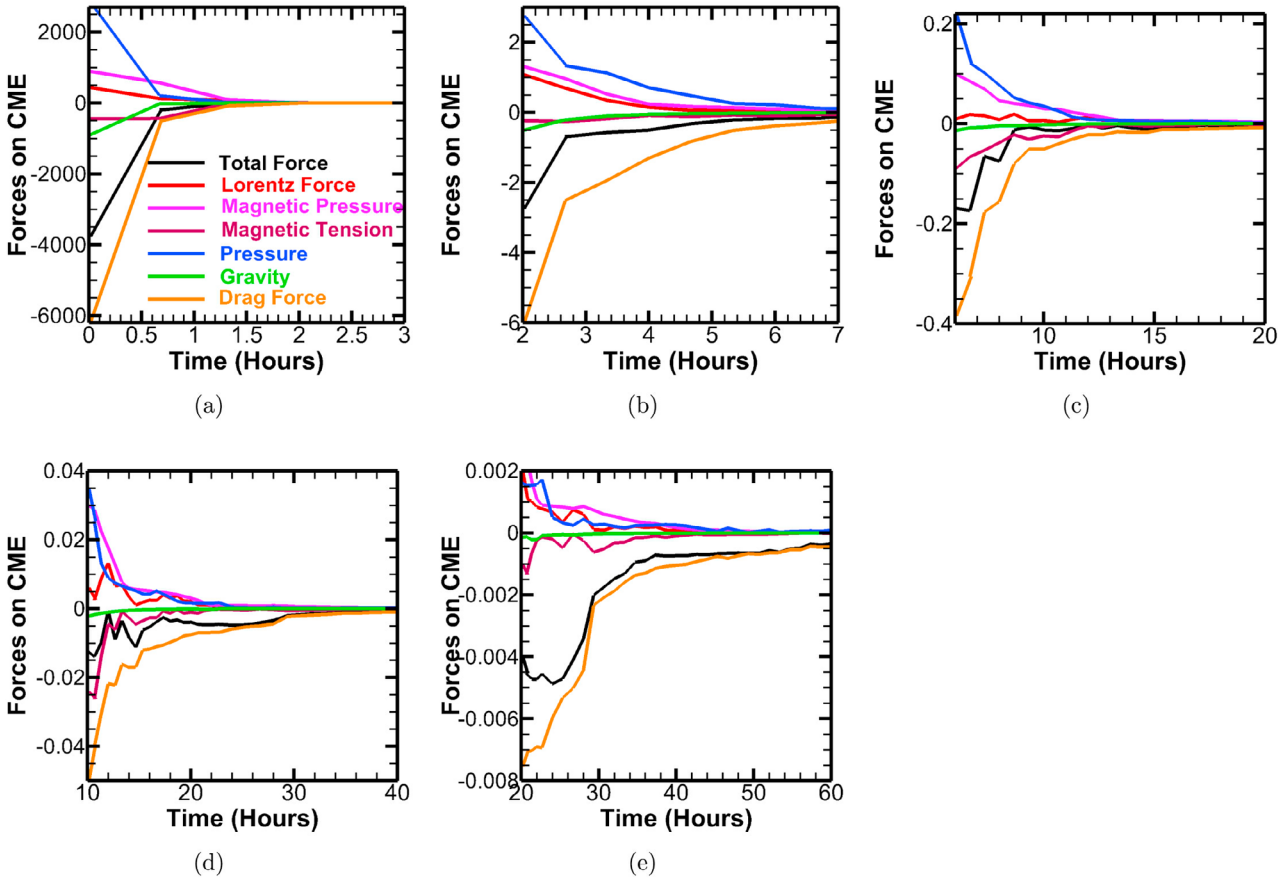

Figure 3. Forces acting on CME during (a) 0–3 h; (b) 2–7 h; (c) 6–20 h; (d) 10–40 h; and (e) 20–60 h. The units of the forces are 10^{-7} N/km^3. It should be noted that each diagram has its own scale.

speed, thus the total force is negative toward Sun in the initial time, it causes both CMEs to decelerate.

[25] From Figure 5, we find that as CME1 propagates into the heliosphere, all the magnitude of the forces acting on CME1 become much smaller in comparison to the total force during the initiation phase. Because of the interaction between the two CMEs, when the two CMEs get closer and closer around 37 h, the pressure, the velocity and the magnetic field of CME2 are all higher than that of CME1, the pressure, velocity and the magnetic field at the CME1 front will increase because of the momentum and energy transfer from CME2 to CME1. So near 37 h, an obvious bump appears in the pressure and the magnetic pressure; and a dip appears in the drag force and the magnetic tension, based on the definition of the forces. The total force begins

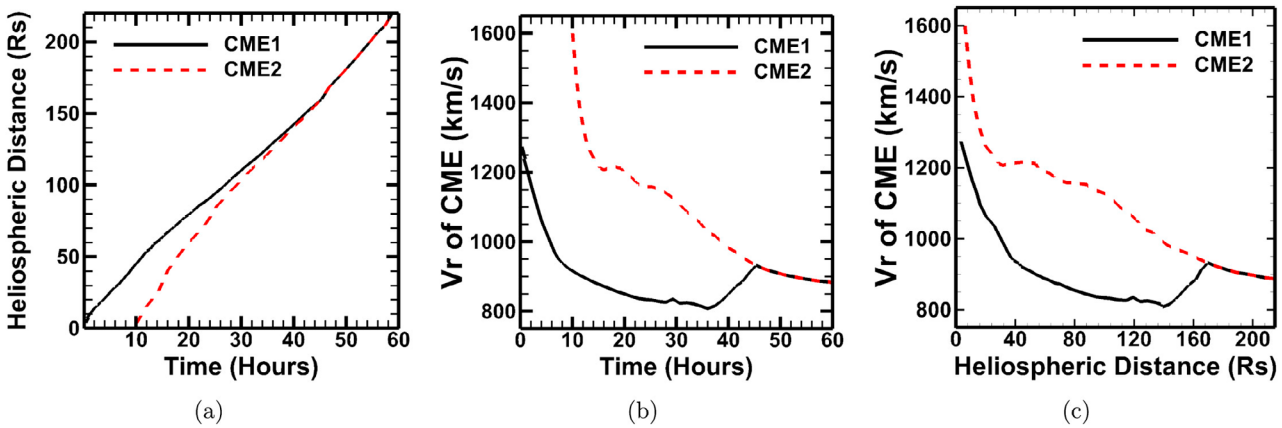

Figure 4. Simulation of (a) CME distance versus time; (b) CME radial speed versus time; and (c) CME radial speed versus distance with the effects of interaction.

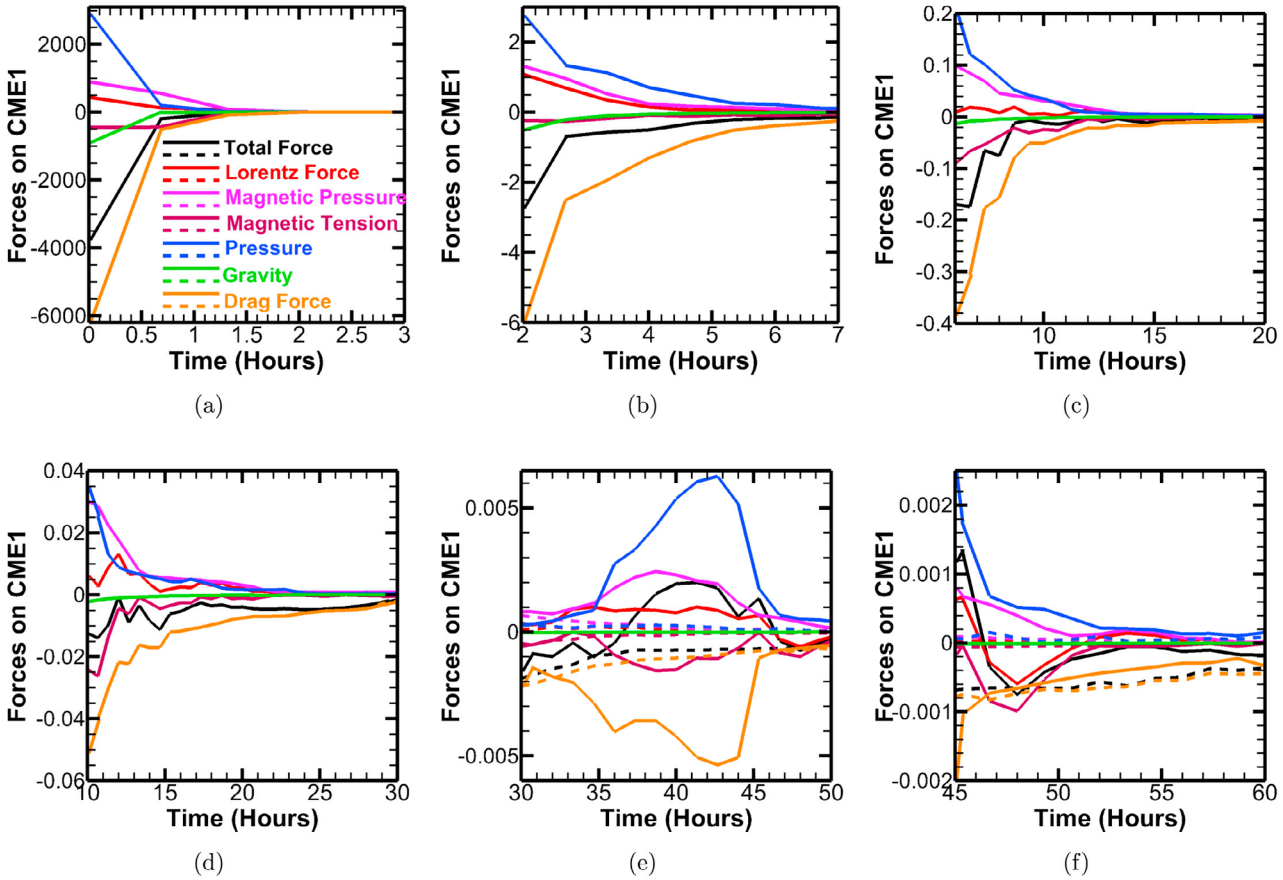

Figure 5. Forces acting on CME1 during (a) 0–3 h; (b) 2–7 h; (c) 6–20 h; (d) 10–30 h; (e) 30–50 h; and (f) 45–60 h. The units of the forces are 10^{-7} N/km^3. It should be noted that each diagram has its own scale. Shown are with the effects of CME2 (solid lines) and single CME1 (dashed lines).

to turn from negative to positive, which is consistent with the speed curve in Figure 4.

[26] It should be noted that the dashed lines in Figure 5a–5f show the forces acting on the single CME1 at different time intervals, without the effects of CME2. In the early stage (i.e., Figures 5a–5c), the solid lines and the dashed lines are identical, which means that the two CMEs interaction has not engaged yet as shown in Figure 4. From the difference between the solid lines and the dashed lines of the two cases, we find that the total force of the single CME case remains negative from t = 0 to 60 h, and the CME speed keeps declining. While in the interaction case, CME1 begins to accelerate and the total force changes from negative to positive near 37 h. This can be explained by the momentum transfer between the two CMEs. In the interaction case, when the two CMEs get closer and closer around 37 h, while the CME1 speed is less than the CME2 speed, the CME1 gains momentum from CME2, so CME1 begins to accelerate after 37 h.

[27] In Figure 6, also shows that all the forces acting on CME2 declined rapidly as CME2 propagates into the heliosphere, and the total force begins to turn from negative to positive near 15 h, which happens much earlier than that for CME1, it can be noted from Figure 6c. It should be mentioned that there exist differences between the two CMEs; when CME1 propagates into the background solar wind, it removes some of the background's mass. Therefore, CME2 does not propagate into the original background solar wind, but into a disturbed medium, less dense, faster and more magnetized [*Lugaz et al.*, 2005; *Xiong et al.*, 2009]. As shown in Figure 6c the positive total force lasted only for about 5 h, and then turned into negative again, which is consistent with the small dip around 16 h in the speed-time curve of Figure 4. The total force remained negative until near 40 h. After 40 h, the total force becomes positive, lasting for no more than 10 h, and then turns negative. From the corresponding speed-time curve in Figure 4, we find that the speed keeps on decreasing and the slope of the curve is also decreased. From Figure 6e, we notice that between 34 and 37 h, there is a significant negative contribution of the Lorentz force to the total force acting on CME2, and the magnetic pressure keep on decrease while the magnetic tension has an obvious dip between 32 and 38 h which is probably because that the shape of the flux rope behind the shock of CME2 changed obviously after the interaction of CME1 and CME2, as shown in Figure 7, which describe the 3D flux rope of CME2 at 32 h (a) and 38 h (b), respectively. This kind of negative magnetic force contributing to the deceleration of CME during the CME-CME interaction event was also reported by *Temmer et al.* [2012].

[28] The dashed lines in Figures 6a–6e show the forces acting on the single CME2 during different time intervals,

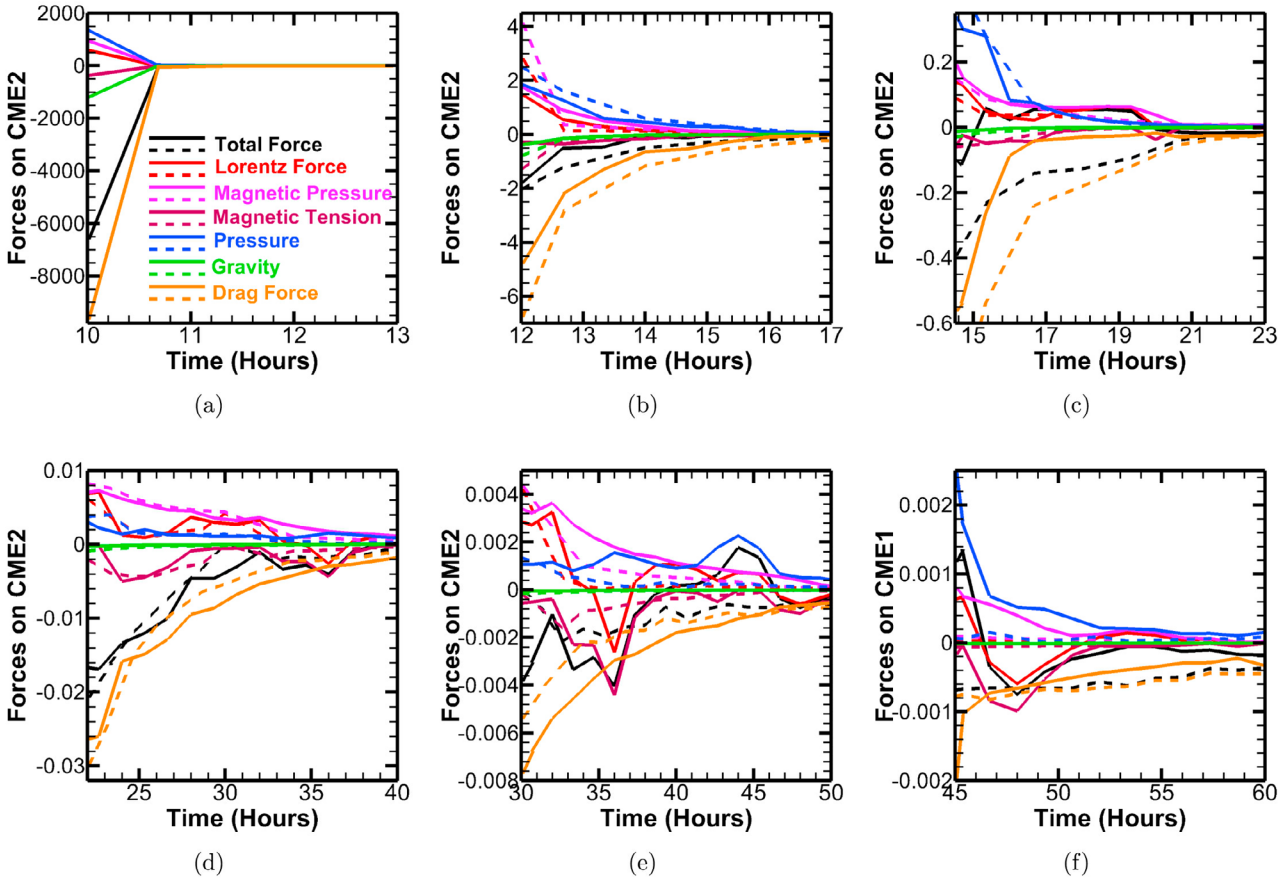

Figure 6. Forces acting on CME2 during (a) 10–13 h; (b) 12–17 h; (c) 15–23 h; (d) 22–40 h; (e) 30–50 h; and (f) 45–60 h. The units of the forces are 10^{-7} N/km^3. It should be noted that each diagram has its own scale. Shown are with the effects of CME1 (solid lines) and single CME2 (dashed lines).

without interaction with CME1. It should note in Figure 6a, the solid lines and dashed lines are identical at the first hour, because these two CMEs have not engaged yet, which also can be indicated by the shock front distance versus time curve (Figure 10a). From the difference between the two cases, we find that the total force of a single CME case remains negative, and the CME speed keeps on declining. In the interaction case, the total force of CME2 remains negative

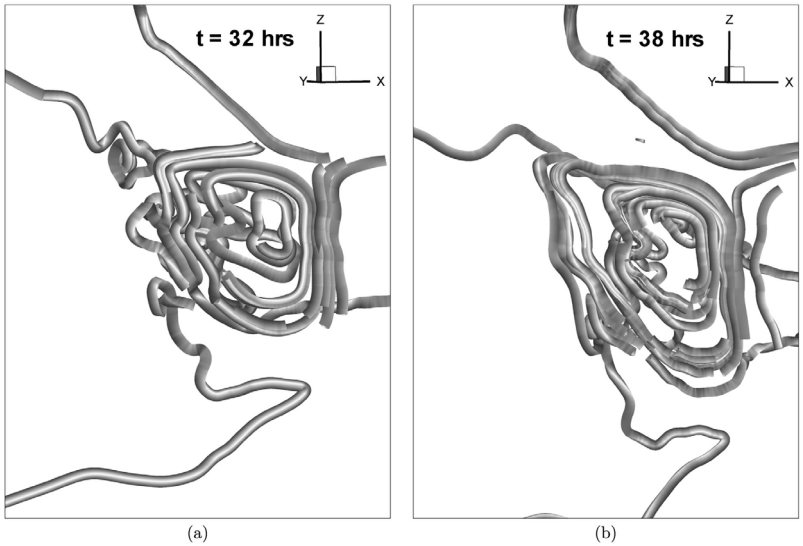

Figure 7. Three-dimensional flux rope of CME2 at (a) t = 32 h and (b) t = 38 h, respectively.

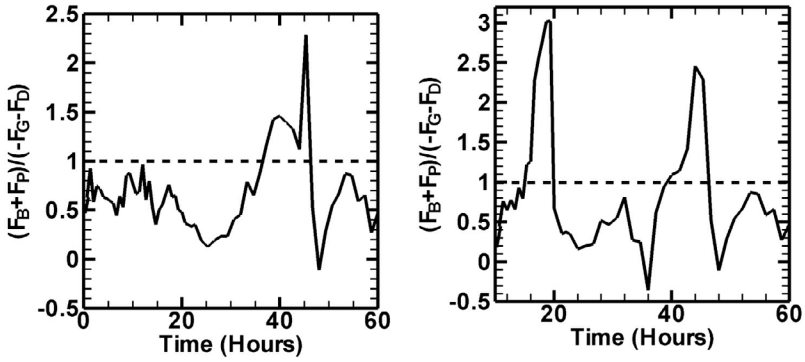

Figure 8. Temporal evolution of the ratio of the Lorentz force and the thermal pressure force to the aerodynamic drag force and the gravitational force of (a) CME1 and (b) CME2 with effects of interaction.

most of the time, and it turns to positive mainly around 18 and 40 h, which corresponds with the small bump of the speed and the decrease of the slope in the speed-time curve.

[29] In order to understand further the acceleration and deceleration of these two CMEs, we have plotted the temporal evolution of the ratio of the Lorentz force and the thermal pressure force to the aerodynamic drag force and the gravitational force of (a) CME1 and (b) CME2, as shown in Figure 8. Frequently, the sum of the forces which contributed to the deceleration is more pronounced than the forces which contributed to the acceleration for CME1 and CME2, as demonstrated in this simulation shown in Figure 8.

[30] To study the interaction between the two CMEs, we made a comparison of the simulation results for three different cases: double CMEs, CME1 only and CME2 only, with all other conditions remaining the same.

[31] Figure 9 and 10 give the temporal evolution of (a) the CME time-distance curve (b) the radial velocity as a function of time, (c) the acceleration/deceleration as a function of time, and (d) the acceleration/deceleration-speed profile, for CME1 and CME2, respectively, with and without interaction.

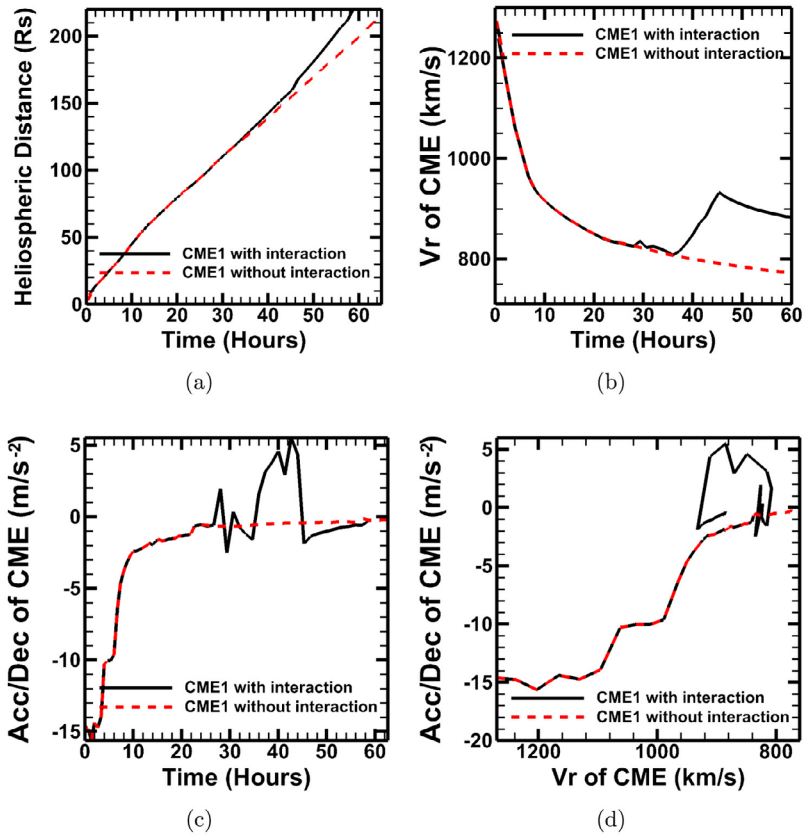

Figure 9. (a) The distance-time profile; (b) the speed-time profile; (c) the acceleration-time profile; and (d) the acceleration-speed profile of CME1 with and without interaction.

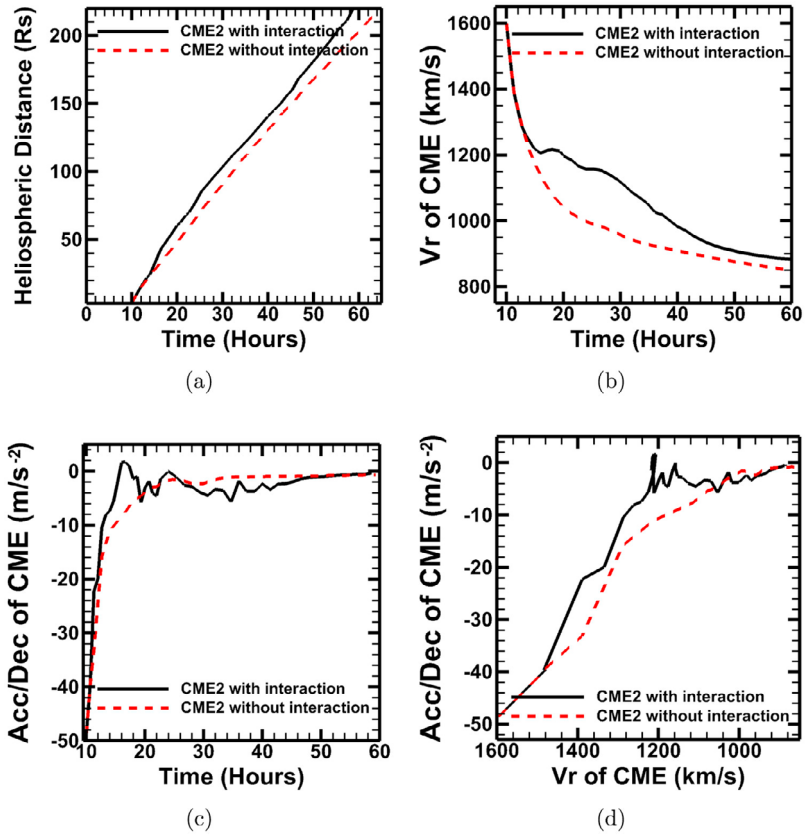

Figure 10. (a) The distance-time profile; (b) the speed-time profile; (c) the acceleration-time profile; and (d) the acceleration-speed profile of CME2 with and without interaction.

In Figure 9, the front of CME1 in the interaction case moves faster than that in the noninteraction case, and the influence of CME2 to the moving speed of the CME1 front primarily happens after time $t = 40$ h, when the shock of CME2 overtakes the shock of CME1 and merges into a combined shock. Figure 9c and 9d, clearly indicates that the effects of interaction causes the change from deceleration to acceleration. After the period of interaction, CME1 appears to decelerate because the speed of CME1 is still faster than the background solar wind speed. It is worth to note that the relationship of radial velocity and acceleration/deceleration shows a complex feature in Figure 9d, this feature could be attributed to interaction of two CMEs as also indicated in Figures 9b and 9c.

[32] In Figure 10 the difference between the two curves happens much earlier than in Figure 9. After 10 h, the heliocentric distance of the CME2 front for the interaction case increases more quickly than that of a single CME2. This is probably because when CME1 propagates into the background solar wind, the property of the solar wind has been disturbed, namely, some of the mass has been removed and the magnetic field also changes. As a consequence, CME2 does not propagate into the original background solar wind but into a disturbed solar wind medium.

[33] By comparison with observational deduced total force given by *Gopalswamy et al.* [2000], the dashed lines in Figure 11 and Figure 12 show the forces acting on a unit volume of CME1 and CME2 with density ρ which could be defined by $F_{\text{gopal}} = \rho a$. Here a is the acceleration of the CMEs, then, we obtain:

$$a = 1.41 - 0.0035u, \tag{5}$$

where a is expressed in m/s^2 and u in km/s. The solid lines in Figure 11 and 12 denote the total forces acting on a unit volume for CME1 and CME2 in our simulation. The forces deduced from Gopalswamy's expression (equation (5)) is simply by multiplying the density at a specific time and space with the acceleration ($F_{\text{gopal}} = \rho a$). In their expression, they did not specifically indicate whether it was a single CME or multiple CMEs, but, these effects should have been included in the observed velocity. As pointed out by *Gopalswamy et al.* [2000], if $a = 0$ in equation (5), a critical speed $u_c = 405$ km/s can be obtained, which is remarkably close to the asymptotic solar wind speed in the equatorial plane. The CMEs speed in our simulation is much faster than u_c, as shown as Figure 6. Therefore, F_{gopal} always remains negative, which can be seen from the dashed lines in Figures 11 and 12. Some qualitative resemblance can be found from these two figures. As shown in Figure 11, the forces acting on CME1 from the two methods almost increase from initiation to 36 h, both have a little bump near 46 h and begin to increase at 48 h. Figure 12 shows that the forces acting on CME2 from the two methods almost

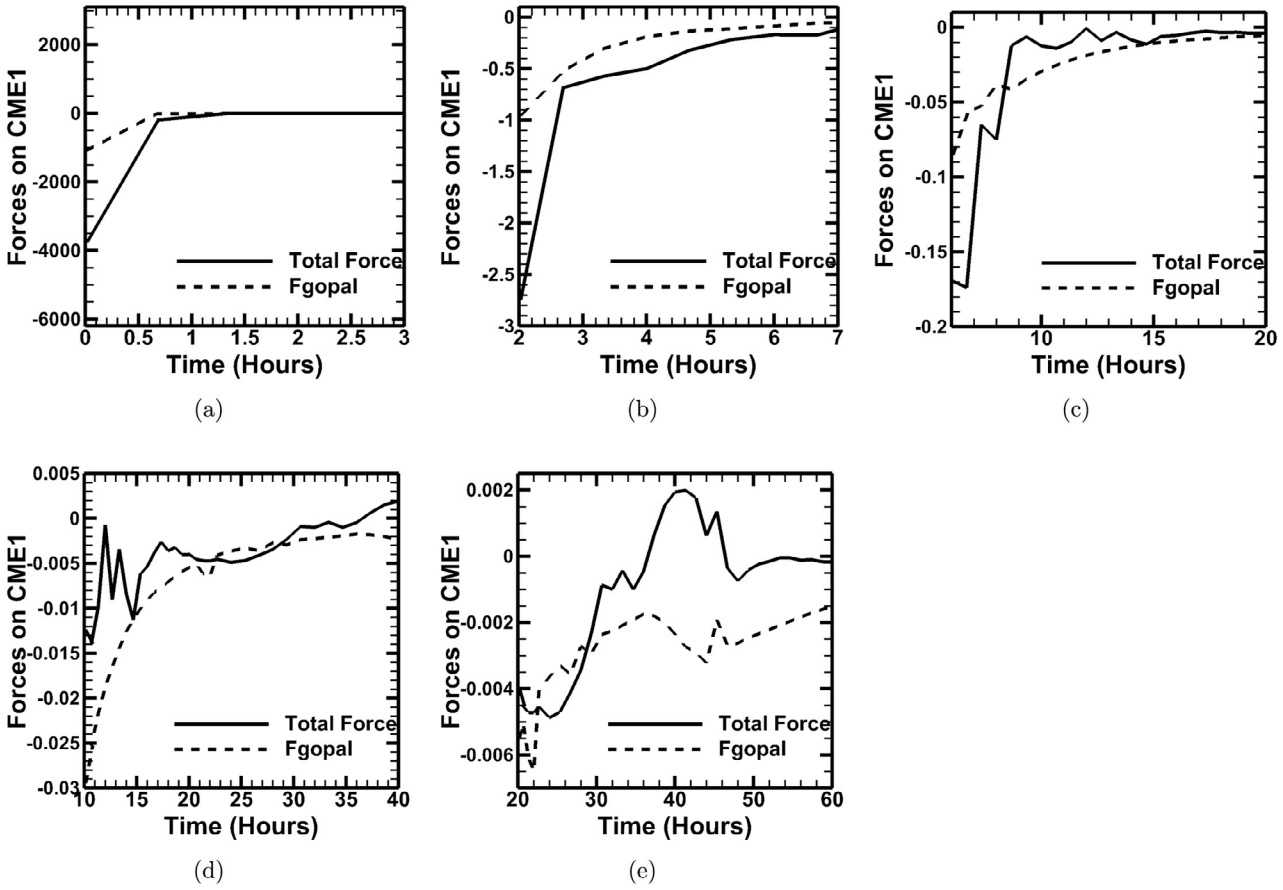

Figure 11. Comparison of the total force acting on CME1 between our simulation with the effects of interaction (solid lines) and deduced Gopalswamy's expression (dashed lines), during (a) 0–3 h, (b) 2–7 h, (c) 6–20 h, (d) 10–40 h, and (e) 20–60 h. The units of the forces are 10^{-7} N/km^3.

increase from initiation to 15 h, from 20 to 30 h, with a little bump around 44 h, and begin to increase at 48 h.

4. Conclusions

[34] We have investigated the acceleration and deceleration of CMEs for the 28–31 March 2001 CME event. A 3D COIN-TVD MHD model was used to simulate the evolution of two interacting CMEs in a realistic ambient solar wind and the two CMEs were initialized by means of two high-density, high-velocity and high-temperature magnetized plasma blob models.

[35] We have analyzed the forces which caused the acceleration and deceleration in detail. The forces which caused the acceleration are magnetic pressure term of the Lorentz force and pressure gradient and the forces which caused the deceleration are aerodynamic drag, magnetic tension and the Sun's gravity. But it shows that the influence of Sun's gravity is at initial stage of CME propagation. The numerical simulation results of the CMEs velocity and the forces acting on the two CMEs are shown in Figures 4 and 6. Figures 4 to 6 clearly show that in CME initiation phase, these two fast CMEs' initial speed were much faster than the ambient solar wind speed, which is a direct consequence of the initiation mechanism we used for this simulation. Both of these two CMEs transfer momentum to the solar wind and they begin to decelerate rapidly. In the meantime, the total force is dominated by the positive pressure gradient and the negative aerodynamic drag force, especially the drag force, and the total force is negative in the early period of time. To study the interaction between the two CMEs, we make a comparison of the simulation result between two CMEs cases, only CME1 and only CME2, with other conditions being the same, as seen from the dashed lines in Figures 5 and 6. It can be demonstrated that in the noninteraction cases, the total force acting on the single CME always remains negative (always decelerated), and the CME speed keep on decreasing, as shown in Figures 9 and 10. The decrease speed is because from beginning to end, the two single CMEs are both fast CMEs, and they transfer momentum to the solar wind at all times.

[36] In the interaction case, we have also investigated the interactions of two CMEs causing the acceleration and deceleration of the CMEs. As CMEs propagate into the heliosphere, all the forces become small. When the two CMEs get closer around 37 h, the CME1 speed is less than CME2 speed, the CME1 gains momentum from CME2, so it begins to accelerate after 37 h, as shown in Figure 4. Near 37 h, we have also found an obvious bump appearing in the pressure curve and the magnetic pressure curve; and a dip appearing in the drag force curve and the magnetic tension curve, and the total force begins to turn from negative to

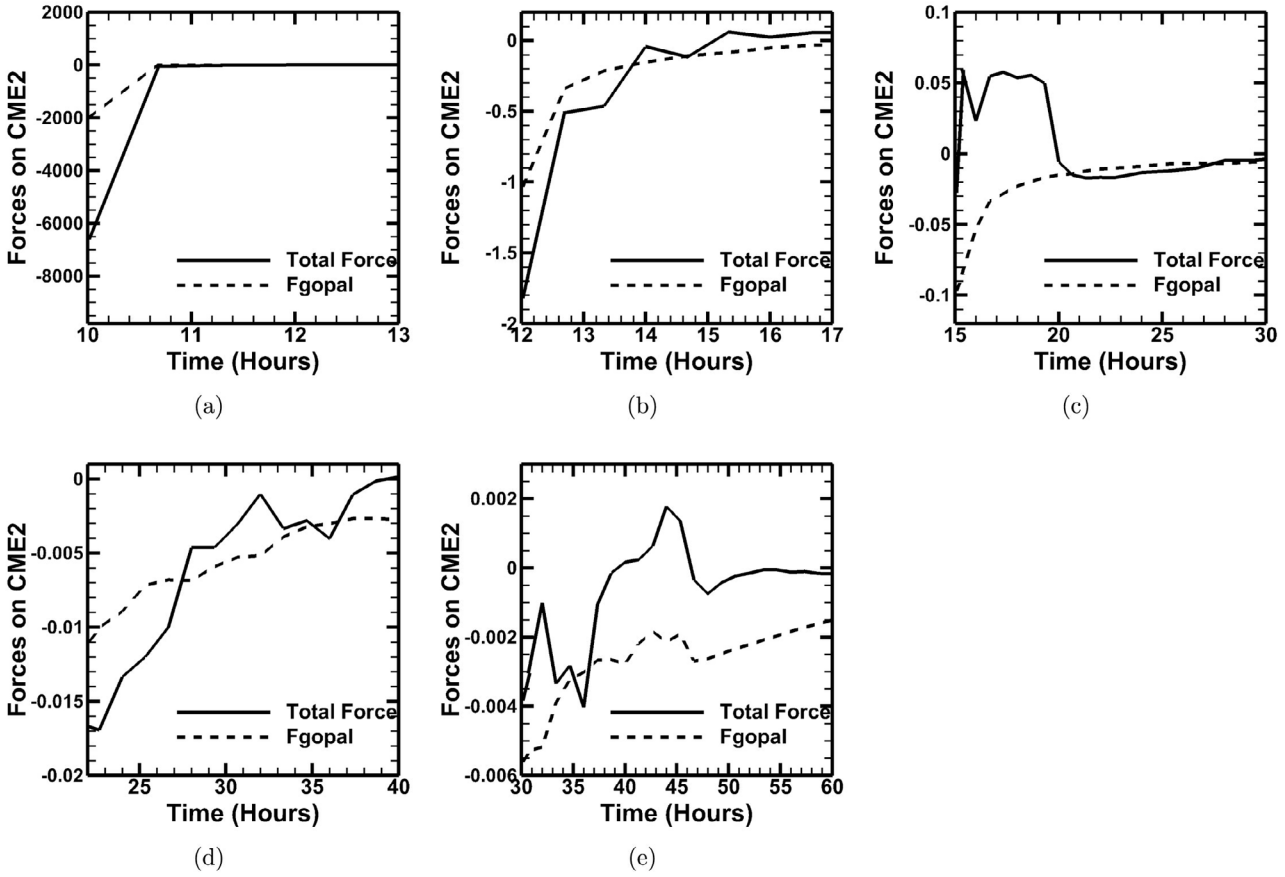

Figure 12. Comparison of the total force acting on CME2 between our simulation with the effects of interaction (solid lines) and Gopalswamy's expression (dashed lines), during (a) 10–13 h, (b) 12–17 h, (c) 15–30 h, (d) 22–40 h, and (e) 30–60 h. The units of the forces are 10^{-7} N/km^3.

positive, as shown in Figure 5e, which is consistent with the speed curve in Figure 4. In summary, we have learned from this simulation which CME propagation is always decelerated. This is obvious because the CME has carried out tremendous momentum until it slows down to the ambient solar wind speed, and then it glides through the heliosphere with at speed of the solar wind. But the CME does exhibit a period of acceleration when the two CMEs interact. From this simulation, the total force at initial stage is few orders of magnitude lager than the later stage, this implies the CMEs are carried outward by the solar wind. Thus, the realistic background is very important for the prediction of CME arrival time.

[37] It should be pointed out that from choosing the density 50% above background as the criteria, we track the sheath of the CME instead of the CME itself. Since the magnetic ejecta (when the density becomes lower due to the expansion of the ejecta) is mostly excluded in the feature tracked, the various forces calculated apply mainly to the sheath region, which may lead to the underestimation of the forces under consideration. But the CME front identified by choosing the location with a maximum velocity in front of the flux-rope is absolutely situated inside the CME region according to our definition, as shown in Figure 1. It is noted that the identified structure might be different if the feature is tracked by other criteria. For instance, magnetic ejecta would be the outstanding feature if plasma beta is used. If the criterion depends on velocity, the tracked feature would be the sheath region and the front-part of the ejecta. Different criteria would surely result in drastically different results, but it is difficult to differentiate various features. It also should be mentioned that the forces analyzed are the forces at the nose of the CMEs. And these forces cannot be assumed as constant throughout the CME.

[38] Finally, a remaining interesting question is: what will happen if we consider different kinds of polarity plasma blob models to simulate the two CMEs interaction events, instead of the normal CME1 and inverse CME2 studied in this paper? Magnetic reconnection may play a somewhat different role, is a topic that will be the focus of a future study.

[39] **Acknowledgments.** This work is jointly supported by the National Basic Research Program of China under grant 2012CB825601, the Chinese Academy of Sciences (KZZD-EW-01-4), the National Natural Science Foundation of China (41031066, 41074121, 40890162, 40921063, 41174150, and 41274192), the Specialized Research Fund for State Key Laboratories and the Public Science and Technology Research Funds Projects of Ocean (201005017). S. T. Wu is supported by AFOSR grant FA9550-07-1-0468, NSF grant ATM-0754378 and AGS-1153323. C.-C. Wu is supported by the NRL 6.1 program. We thank the SOHO/LASCO team for letting us use their data. SOHO is a mission of international collaboration between ESA and NASA. The Wilcox Solar Observatory (WSO) data used in this study were obtained via the Web site http://wso.stanford.edu/synopticl.html for CR 1974. The WSO is currently supported by NASA.

[40] Philippa Browning thanks the reviewers for their assistance in evaluating this paper.

References

Andrews, M. D., and R. A. Howard (2001), A two-type classification of Lasco coronal mass ejection, *Space Sci. Rev.*, *95*(1/2), 147–163.

Borgazzi, A., A. Lara, E. Echer, and M. V. Alves (2009), Dynamics of coronal mass ejections in the interplanetary medium, *Astron. Astrophys.*, *498*, 885–889, doi:10.1051/0004-6361/200811171.

Burlaga, L. F., Plunkett, S. P., and St. Cyr, O. C. (2002), Successive CMEs and complex ejecta, *J. Geophys. Res.*, *107*(A10), 1266, doi:10.1029/2001JA000255.

Cargill, P. J. (2004), On the aerodynamic drag force acting on interplanetary coronal mass ejections, *Sol. Phys.*, *221*, 135–149, doi:10.1023/B:SOLA.0000033366.10725.a2.

Cargill, P. J., J. Chen, and D. A. Garren (1994), Oscillations and evolution of curved current-carrying loops in the solar corona, *Astrophys. J.*, *423*, 854, doi:10.1086/173863.

Cargill, P. J., J. Chen, D. S. Spricer, and S. T. Zalesak (1996), Magnetohydrodynamic simulations of the motion of magnetic flux tubes through a magnetized plasma, *J. Geophys. Res.*, *101*, 4855–4870, doi:10.1029/95JA03769.

Chané, E., C. Jacobs, B. Van der Holst, S. Poedts, and D. Kimpe (2005), On the effect of the initial magnetic polarity and of the background wind on the evolution of CME shocks, *Astron. Astrophys.*, *432*, 331–339, doi:10.1051/0004-6361:20042005.

Chané, E., B. Van der Holst, C. Jacobs, S. Poedts, and D. Kimpe (2006), Inverse and normal coronal mass ejections: Evolution up to 1 AU, *Astron. Astrophys.*, *447*, 727–733, doi:10.1051/0004-6361:20053802.

Chané, E., S. Poedts, and B. Van der Holst (2008), On the combination of ACE data with numerical simulations to determine the initial characteristics of a CME, *Astron. Astrophys.*, *492*, L29–L32.

Chen, J. (1989), Effects of toroidal forces in current loops embedded in a background plasma, *Astrophys. J.*, *338*, 453–470.

Chen, J. (1996), Theory of prominence eruption and propagation: Interplanetary consequences, *J. Geophys. Res.*, *101*, 27,499–27,519, doi:10.1029/96JA02644.

Chen, J., and J. Krall (2003), Acceleration of coronal mass ejections, *J. Geophys. Res.*, *108*(A11), 1410, doi:10.1029/2003JA009849.

Feng, X., et al. (2003), A class of two-step TVD MacCormack type numerical scheme for MHD equations, *Chin. J. Space Sci.*, *23*, 401–412.

Feng, X., et al. (2005), A comparative study on 3-D solar wind structure observed by Ulysses and MHD simulation, *Chin. Sci. Bull.*, *50*(7), 672–678, doi:10.1360/982004-293.

González-Esparza, A., A. Lara, E. Perez-Tijerina, A. Santillan, and N. Gopalswamy (2003), A numerical study on the acceleration and transit time of coronal mass ejections in the interplanetary medium, *J. Geophys. Res.*, *108*(A1), 1039, doi:10.1029/2001JA009186.

Gopalswamy, N., A. Lara, R. P. Lepping, M. L. Kaiser, D. Berdichevsky, and O. C. St. Cyr (2000), Interplanetary acceleration of coronal mass ejections, *Geophys. Res. Lett.*, *27*(2), 145–148, doi:10.1029/1999GL003639.

Joshi, A. D., and N. Srivastava (2011), Determination of acceleration from 3D reconstruction of coronal mass ejections observed by STEREO, *Astrophys. J.*, *739*, 8, doi:10.1088/0004-637X/739/1/8.

Low, B. C., and M. Zhang (2002), The hydromagnetic origin of the two dynamical types of solar coronal mass ejections, *Astrophys. J.*, *564*, L53, doi:10.1086/338798.

Lugaz, N., and I. I. Roussev (2011), Numerical modeling of interplanetary coronal mass ejections and comparison with heliospheric images, *J. Atmos. Terr. Phys.*, *73*(10), 1187–1200, doi:10.1016/j.jastp.2010.08.016.

Lugaz, N., W. B. Manchester IV, and T. I. Gombosi (2005), The evolution of coronal mass ejection density structures, *Astrophys. J.*, *627*, 1019, doi:10.1086/430465.

MacQueen, R. M., and R. R. Fisher (1983), The kinematics of solar inner coronal transients, *Sol. Phys.*, *89*, 89–102, doi:10.1007/BF00211955.

Manchester, W., IV, T. Gombosi, D. DeZeeuw, and Y. Fan (2004), Eruption of a buoyantly emerging magnetic flux rope, *Astrophys. J.*, *610*(1), 588, doi:10.1086/421516.

Schmidt, J. M., and P. J. Cargill (2000), A model for accelerated density enhancements emerging from coronal streamers in large-angle and spectrometric coronagraph observations, *J. Geophys. Res.*, *105*(A5), 10,455–10,464, doi:10.1029/1999JA900505.

Sheeley, N. R., Jr., T. H. Walter, Y.-M. Wang, and R. A. Howard (1999), Continuous tracking of coronal outflows: Two kinds of coronal mass ejections, *J. Geophys. Res.*, *104*, 24,739–24,767, doi:10.1029/1999JA900308.

Shen, F., X. Feng, S. T. Wu, and C. Xiang (2007), Three-dimensional MHD simulation of CMEs in three-dimensional background solar wind with the self-consistent structure on the source surface as input: Numerical simulation of the January 1997 Sun-Earth connection event, *J. Geophys. Res.*, *112*, A06109, doi:10.1029/2006JA012164.

Shen, F., X. Feng, and W. B. Song (2009), An asynchronous and parallel time-marching method: Application to the three-dimensional MHD simulation of the solar wind, *Sci. China Ser. E*, *52*(10), 2895–2902.

Shen, F., X. S. Feng, C. Q. Xiang, and W. B. Song (2010), The statistical and numerical study of the global distribution of coronal plasma and magnetic field near 2.5 Rs over a 10-year period, *J. Atmos. Sol. Terr. Phys.*, *72*(13), 1008–1018, doi:10.1016/j.jastp.2010.05.016.

Shen, F., X. S. Feng, S. T. Wu, C. Q. Xiang, and W. B. Song (2011a), Three-dimensional MHD simulation of the evolution of the April 2000 CME event and its induced shocks using a magnetized plasma blob model, *J. Geophys. Res.*, *116*, A04102, doi:10.1029/2010JA015809.

Shen, F., X. S. Feng, Y. Wang, S. T. Wu, W. B. Song, J. P. Guo, and Y. F. Zhou (2011b), Three-dimensional MHD simulation of two coronal mass ejections' propagation and interaction using a successive magnetized plasma blobs model, *J. Geophys. Res.*, *116*, A09103, doi:10.1029/2011JA016584.

Shen, F., X. S. Feng, and C. Q. Xiang (2012), Improvement to the global distribution of coronal plasma and magnetic field on the source surface using expansion factor f_s and angular distance θ_b, *J. Atmos. Sol. Terr. Phys.*, *77*, 125–131, doi:10.1016/j.jastp.2011.12.009.

St. Cyr, O. C., J. T. Burkepile, A. J. Hundhausen, and A. R. Lecinski (1999), A comparison of ground-based and spacecraft observations of coronal mass ejections from 1980–1989, *J. Geophys. Res.*, *104*(A6), 12,493–12,506, doi:10.1029/1999JA900045.

St. Cyr, O. C., et al. (2000), Properti/opt/intel/Compiler/11.0/069/bin/intel64es of coronal mass ejections: SOHO LASCO observations from January 1996 to June 1998, *J. Geophys. Res.*, *105*, 18,169–18,185, doi:10.1029/1999JA000381.

Tandberg-Hanssen, E. (1995), *The Nature of Solar Prominences*, *Astrophys. Space Sci. Libr.*, vol. 199, Kluwer, Dordrecht, Netherlands.

Tappin, S. (2006), The deceleration of an interplanetary transient from the Sun to 5 Au, *Sol. Phys.*, *233*(2), 233–248, doi:10.1007/s11207-006-2065-2.

Temmer, M., et al. (2012), Characteristics of kinematics of a coronal mass ejection during the 2010 August 1 CME-CME interaction event, *Astrophys. J.*, *749*(1), 57.

Tóth, G. (2000), The $\nabla \cdot \vec{B} = 0$ constraint in shock-capturing magnetohydrodynamics codes, *J. Comput. Phys.*, *161*, 605–652.

Vourlidas, A., R. A. Howard, E. Esfandiari, S. Patsourakos, S. Yashiro, and G. Michalek (2010), Comprehensive analysis of coronal mass ejection mass and energy properties over a full solar cycle, *Astrophys. J.*, *722*, 1522, doi:10.1088/0004-637X/722/2/1522.

Vršnak, B. (2006), Forces governing coronal mass ejections, *Adv. Space Res.*, *38*, 431–440, doi:10.1016/j.asr.2005.03.090.

Vršnak, B., and N. Glpalswamy (2002), Influence of the aerodynamic drag on the motion of interplanetary ejecta, *J. Geophys. Res.*, *107*(A2), 1019, doi:10.1029/2001JA000120.

Vršnak, B., et al. (2012), Propagation of interplanetary coronal mass ejections: The drag-based model, *Solar Phys.*, doi:10.1007/s11207-012-0035-4, in press.

Wang, Y. M., S. Wang, and P. Z. Ye (2002), Multiple magnetic clouds in interplanetary space, *Sol. Phys.*, *211*, 333–344, doi:10.1023/A:1022404425398.

Wang, Y. M., P. Z. Ye, and S. Wang (2003), Multiple magnetic clouds: Several examples during March–April, 2001, *J. Geophys. Res.*, *108*(A10), 1370, doi:10.1029/2003JA009850.

Wang, Y., H. Zheng, S. Wang, and P. Ye (2005), MHD simulation of the formation and propagation of multiple magnetic clouds in the heliosphere, *Astron. Astrophys.*, *434*, 309–316, doi:10.1051/0004-6361:20041423.

Wei, F. S., X. S. Feng, H. C. Cai, and Q. J. Zhou (2003), Global distribution of coronal mass outputs and its relation to solar magnetic field structures, *J. Geophys. Res.*, *108*(A6), 1238, doi:10.1029/2002JA009439.

Wu, S. T., and W. P. Guo (1997), A self-consistent numerical magnetohydrodynamic (MHD) model of helmet streamer and flux-rope interactions: Initiation and propagation of coronal mass ejections (CMEs), in *Coronal Mass Ejections*, *Geophys. Monogr. Ser.*, vol. 99, edited by N. Crooker, J. A. Joselyn, and J. Feynman, pp. 83–89, AGU, Washington, D. C., doi:10.1029/GM099p0083.

Wu, S. T., et al. (2004), Numerical magnetohydrodynamic experiments for testing the physical mechanisms of coronal mass ejections acceleration, *Sol. Phys.*, *225*, 157–175, doi:10.1007/s11207-004-2568-7.

Wu, S. T., et al. (2005), The role of magnetic reconnection in CME acceleration, *Space Sci. Rev.*, *121*(1–4), 33–47, doi:10.1007/s11214-006-6159-9.

Xiong, M., H. Zheng, and S. Wang (2009), Magnetohydrodynamic simulation of the interaction between two interplanetary magnetic clouds and its consequent geoeffectiveness: 2. Oblique collision, *J. Geophys. Res.*, *114*, A11101, doi:10.1029/2009JA014079.